

# Giant anomalous Hall effect and band folding in a Kagome metal with mixed dimensionality

Erjian Cheng<sup>1,#,\*</sup>, Kaipu Wang<sup>2,#</sup>, Simin Nie<sup>3</sup>, Tianping Ying<sup>4</sup>, Zongkai Li<sup>2</sup>, Yiwei Li<sup>5</sup>, Yang Xu<sup>6</sup>, Houke Chen<sup>7</sup>, Ralf Koban<sup>1</sup>, Horst Borrmann<sup>1</sup>, Walter Schnelle<sup>1</sup>, Vicky Hasse<sup>1</sup>, Meixiao Wang<sup>2</sup>, Yulin Chen<sup>2,7</sup>, Zhongkai Liu<sup>2,\*</sup> and Claudia Felser<sup>1,\*</sup>

<sup>1</sup> Max Planck Institute for Chemical Physics of Solids, 01187 Dresden, Germany

<sup>2</sup> School of Physical Science and Technology, ShanghaiTech Laboratory for Topological Physics, ShanghaiTech University, 201210 Shanghai, China

<sup>3</sup> Department of Mechanical Engineering, Stanford University, 94305 Stanford, California, USA

<sup>4</sup> Institute of Physics and University of Chinese Academy of Sciences, Chinese Academy of Sciences, 100190 Beijing, China

<sup>5</sup> Institute for Advanced Studies (IAS), Wuhan University, 430072 Wuhan, China

<sup>6</sup> Key Laboratory of Polar Materials and Devices (MOE), School of Physics and Electronic Science, East China Normal University, 200241 Shanghai, China

<sup>7</sup> Department of Physics, University of Oxford, Oxford OX1 3PU, UK

## Abstract

Magnetic metals with geometric frustration offer a fertile ground for studying novel states of matter with strong quantum fluctuations and unique electromagnetic responses from conduction electrons coupled to spin textures. Recently, TbTi<sub>3</sub>Bi<sub>4</sub> has emerged as such an intriguing platform as it behaves as a quasi-one-dimension (quasi-1D) Ising magnet with antiferromagnetic orderings at 20.4 K and 3 K, respectively. Magnetic fields along the Tb zigzag-chain direction reveal plateaus at 1/3 and 2/3 of saturated magnetization, respectively. At metamagnetic transition boundaries, a record-high anomalous Hall conductivity of  $6.2 \times 10^5 \Omega^{-1} \text{cm}^{-1}$  is observed. Within the plateau, noncollinear magnetic texture is suggested. In addition to the characteristic Kagome 2D electronic structure, ARPES unequivocally demonstrates quasi-1D electronic structure from the Tb 5d bands and a quasi-1D hybridization gap in the magnetic state due to band folding with  $q = (1/3, 0, 0)$  possibly from the spin-density-wave order along the Tb chain. These findings emphasize the crucial role of mixed dimensionality and the strong coupling between magnetic texture and electronic band structure in regulating physical properties of materials, offering new strategies for designing materials for future spintronics applications.

## Introduction

Geometrically frustrated magnets with various structures provide a promising platform for novel states of matter with emerging collective behaviors and strong quantum fluctuations [1–4]. Recently, kagome-based metals have risen to prominence due to their topological electronic structures, structural instabilities, accompanied by significant electromagnetic and transport properties [5–10]. Particularly noteworthy is the coupling between conduction electrons and spin textures in magnetic metallic compounds, leading to anomalous transport phenomena such as the anomalous Hall effect (AHE) with time reversal symmetry breaking [5–10]. Unlike the ordinary Hall effect, which is caused by the Lorentz force bending charge carriers perpendicular to a magnetic field, the AHE due to magnetic texture is most often associated with finite scalar spin chirality  $\chi_{ijk} = \mathbf{S}_i \cdot (\mathbf{S}_j \times \mathbf{S}_k)$ , where  $\mathbf{S}_i$  are spins [5]. Additionally, it has been demonstrated that the AHE can distinguish near-degenerate states linked by an emergent discrete symmetry operation under finite magnetic fields [7]. It also elucidates the interplay between magnetism and the topological aspects of band structure [5, 11–13], establishing AHE as an effective approach to study the coupling between magnetism and electronic band structure.

In magnetic kagome metals, the magnetic texture and electronic band structure predominantly exhibit quasi-two-dimensional (quasi-2D) or quasi-three-dimensional (quasi-3D) characteristics [5–10]. However, systems involving lower dimensionality (1D) are less studied. Spin zigzag chains, as fundamental models, have long intrigued theoreticians due to their unique properties. Strong quantum fluctuations in one dimension can lead to the absence of finite-temperature phase transitions and the breakdown of Landau’s Fermi liquid theory, making 1D systems distinctive in many aspects [14,15]. Additionally, 1D many-body physics allows for exact solutions in certain microscopic models [14,15]. Therefore, studying 2D Kagome systems with (quasi-)1D spin chains is particularly interesting for exploring how magnetism interacts with electronic band structure and the extent to which transport properties are affected by their coupling.

Very recently, the newly synthesized titanium-based bilayer kagome metal  $LnTi_3Bi_4$  ( $Ln = La, Ce, Pr, Nd, Sm, Eu, Gd, Yb$ ) have been reported, showing tunable magnetism by rare-earth engineering [16–21].  $LnTi_3Bi_4$  crystallizes in an orthorhombic structure with the  $Fmmm$  (No. 69) space group [16]. This structure comprises alternating layers of  $Ti_3Bi_4$ ,  $LnBi_2$ , and Bi along the  $c$  axis. Unlike the  $D_{6h}$

symmetry observed in kagome metals  $AM_3Sb_5$  (where  $A = K, Rb, Cs, M = V, Ti$ ) [22–24], the quasi-1D nature of the  $Ln$  zigzag chains running along the  $a$  axis leads to an orthorhombic structure in the  $TbBi_2$  layer, resulting in a reduced crystalline symmetry ( $D_{2h}$ ). Motivated by the coexistence of quasi-2D Kagome bilayers, quasi-1D zigzag chains, and tunable magnetism in  $LnTi_3Bi_4$ , we successfully synthesized  $TbTi_3Bi_4$ , a new member sharing the same crystal structure as the  $LnTi_3Bi_4$  family, as illustrated in Figs. 1a, 1b and 1c. In this work, based on transport and ARPES experiments, we show that both the magnetism and electronic band structure with mixed dimensionality, and the coupling between them play a crucial role in regulating the physical properties of  $TbTi_3Bi_4$ .

### **Magnetic ordering and transport properties of $TbTi_3Bi_4$**

Figure 1d displays the magnetization with magnetic field applied in different orientations, a sudden decline at 20.4 K can be clearly distinguished for all axis, which corresponding to the first magnetic ordering ( $T_{N1}$ ). For magnetic field along the  $a$  axis, the second magnetic ordering ( $T_{N2}$ ) can be resolved at 3 K. These two magnetic transitions have been confirmed in specific heat (Supplementary Fig. S1a). The fit to the inverse magnetic susceptibility shows antiferromagnetic coupling for magnetic field parallel to  $b$  and  $c$  axis, and ferromagnetic coupling for the  $a$  axis, suggestive of strong magnetic anisotropy of  $TbTi_3Bi_4$  (Supplementary Fig. 1b). Figure 1e shows the field-dependent magnetization (MH) profiles at 2 K for different orientations. As observed, the magnetization exhibits linear behavior for the  $b$  and  $c$  axis, while it saturates beyond 3 T for the  $a$  axis. Below this threshold, there are two distinct hysteresis loops and a 1/3 magnetization plateau evident. To scrutinize the magnetization behavior along the zigzag chain direction, the temperature-dependent magnetization in various fields has been conducted, as shown in Fig. 1f. Surprisingly, in addition to 1/3 magnetization plateau, another weaker plateau located at 2/3 magnetization can be recognized. Fractional magnetization plateaus in quantum magnets signal geometrical frustration in the system [7,14,15]. Observing these plateaus in  $TbTi_3Bi_4$  implies strong quantum fluctuations, prompting further investigation into the transport properties.

Figure 1h displays the longitudinal resistivity, featuring overall metallic behavior. It is worthy to note that the temperature dependence of resistivity at high temperature is quite linear, implying a possible strange metal behavior in  $TbTi_3Bi_4$  [25]. At  $T_{N1}$ , resistivity declines suddenly, while it reaches

a minimum at  $T_{N2}$ , below which the resistivity slightly increases, suggestive of a possible gap opening after magnetic transitions. The magnetic ordering effect on transport is more prominent in temperature-dependent Seebeck coefficient (Supplementary Fig. 2a). To check if there are any charge modulations from structural instabilities induced by a charge density wave (CDW), scanning tunneling microscopy (STM) experiments have been conducted, as shown in Fig. 1g. However, down to 0.35 K, such charge modulations from the topography mapping from the Tb terminated surface cannot be resolved, and therein, we propose that only a magnetic- relevant scenario may be at play. The magnetoresistance (MR) and transverse Hall resistivity with different measured configurations at 2 K are shown in Figs. 1i and 1j. When magnetic field is applied along the  $c$  axis, MR shows a large and positive value of  $\sim 150\%$  at 9 T for both current applied along the  $a$  and  $b$  axis, bearing weak quantum oscillations (QOs) above  $\sim 6$  T (also evident in Hall resistivity). As a contrast, Seebeck coefficient shows very conspicuous QOs (Supplementary Fig. 2b). Analysis of the oscillating components shows that a small Fermi pocket comprises of massless Dirac fermions derived from Ti kagome lattices near  $E_F$  plays a key role in transport, and the magnetic ordering from Tb zigzag chains intertwines with it (see Supplementary Note 2 for more details).

When applying magnetic field parallel to the  $a$  axis, intriguingly, the MR shows a negative value of  $-50\%$ , featuring multiple anomalies, which is more prominent in Hall resistivity. By carefully comparing the longitudinal and transverse resistivity with magnetization, these anomalies are verified from multiple metamagnetic transitions of  $\text{TbTi}_3\text{Bi}_4$  (Supplementary Fig. 3). It is noteworthy that the negative MR observed in this measurement configuration persists up to 300 K, significantly higher than the highest ordering temperature of approximately 20.4 K (Supplementary Fig. 4a). Negative longitudinal MR is typically attributed to several factors: (i) inhomogeneous current distribution or current jetting effect, (ii) weak localization effects, (iii) the chiral anomaly of Weyl fermions, and (iv) field-induced suppression of scattering from local moments or magnetic impurities [26–28]. Given the measurement configurations and the broad temperature dependence of the negative MR in our experiments, scenarios (i), (ii), and (iii) can be excluded. We therefore suggest that magnetic fluctuations in the paramagnetic state are responsible. However, the observation of negative MR extending to room temperature in  $\text{TbTi}_3\text{Bi}_4$  is very rare, indicating that the spins of Tb along the zigzag chain in  $\text{TbTi}_3\text{Bi}_4$  remain highly dynamic even at very high temperatures.

## Giant anomalous Hall effect in TbTi<sub>3</sub>Bi<sub>4</sub>

To further understand the coupling between magnetism and electronic band structure in TbTi<sub>3</sub>Bi<sub>4</sub>, we examined the low-temperature Hall resistivity. As shown in Fig. 2a, the Hall resistivity displays pronounced hysteresis with a topological-Hall-like effect, consistent with the MH curves (Supplementary Fig. 5). As the temperature increases, the AHE and hysteresis gradually weaken and disappear around 20 K. The Hall resistivity during both the down-sweeping and up-sweeping processes overlaps significantly away from metamagnetic transitions. Therefore, the net anomalous Hall contributions have been extracted using  $\rho_{zy}^A = [\rho_{zy}(+H) - \rho_{zy}(-H)]/2$ , accounting for the antisymmetric behavior of anomalous Hall resistivity at metamagnetic transitions. The calculated data are presented in Supplementary Fig. 4c, with the corresponding contour plot shown in Fig. 2c. For better comparison, the phase diagram of magnetization derived from MH curves is also plotted in Fig. 2b. With decreasing temperature to  $\sim 50$  K, the magnetization displays nonlinear behavior, indicating magnetic fluctuations in the paramagnetic state. Below 20 K, magnetic ordering starts to dominate, the peaks in  $dM/dH$  associated with two successive metamagnetic transitions define the phase boundaries for the three magnetic phases (I, II, and III). The II magnetic phase corresponds to the regime of 1/3 magnetization plateau. The phase diagram of  $\rho_{zy}^A$  (Fig. 2c) is consistent with magnetization. In the plateau regime, the existence area of  $\rho_{zy}^A$  is broad, and resembles the phase diagrams reported in typical skyrmion-hosting materials [29–31], for example, Gd<sub>2</sub>PdSi<sub>3</sub> [31]. Skyrmion lattices are typically reported in chiral, polar, or frustrated magnets, with chiral magnetic structures [29]. The formation of skyrmions and noncollinear spin textures is primarily attributed to two types of magnetic interactions [29]: the antisymmetric exchange interaction due to spin-orbit coupling, known as the Dzyaloshinskii–Moriya (DM) interaction [32], and itinerant-electron-mediated long-range interactions that cause magnetic frustration, known as the Ruderman–Kittel–Kasuya–Yosida (RKKY) interaction. Due to the high symmetries of the space group of TbTi<sub>3</sub>Bi<sub>4</sub>, the nearest and next-nearest exchange couplings do not allow for the existence of DM interaction [32]; this interaction can only be expected in the next-next-nearest exchange coupling. Alternatively, considering the quasi-1D spin zigzag chains in TbTi<sub>3</sub>Bi<sub>4</sub>, a frustration scenario may be at play. Consequently, in the plateau regime, the magnetic texture cannot remain quasi-1D; it must allow for a chiral magnetic structure and the existence of a skyrmion phase. To identify this, neutron scattering or X-ray experiments are anticipated.

In TbTi<sub>3</sub>Bi<sub>4</sub>, the coupling between magnetism and electronic band structure give rise to giant AHE. As discussed in Fig. 2(a), in the magnetic state, distinct AHE has been observed. At 2 K, the largest magnitude of  $\rho_{zy}^A$  is 0.894  $\mu\Omega$  cm, which is comparable to the skyrmion-hosting material Gd<sub>2</sub>PdSi<sub>3</sub>

of  $2.6 \mu\Omega \text{ cm}$  [31] and Weyl semimetal SmAlSi of  $1.7 \mu\Omega \text{ cm}$  in the  $ac$  plane [34]. We then calculate the longitudinal conductivity, anomalous Hall conductivity (AHC) and anomalous Hall angle (AHA) of TbTi<sub>3</sub>Bi<sub>4</sub> (Supplementary Fig. 4d). Astonishingly, the AHA and AHC are 42% and  $2.5 \times 10^5 \Omega^{-1} \text{ cm}^{-1}$ , respectively, much larger than Gd<sub>2</sub>PdSi<sub>3</sub> and SmAlSi. The AHC is the highest among reported magnets, to the best of our knowledge, as shown in Fig. 2f. To further elaborate the strong electromagnetic responses in TbTi<sub>3</sub>Bi<sub>4</sub>, the angle-dependent Hall resistivity (Fig. 2d) and longitudinal resistivity (Supplementary Fig. 6a) have been measured. The current is applied along the  $a$  axis, and the sample rotates from having the magnetic field parallel to the  $b$  axis to parallel with the  $a$  axis, as shown in the inset of Fig. 2d. When the magnetic field deviates from the  $b$ -axis by  $10^\circ$ , a broad hysteresis appears. As the angle increases, this broad hysteresis splits into two distinct loops with sharper peaks. Beyond  $45^\circ$ , the overall transverse and longitudinal resistivity remains relatively unchanged. At  $90^\circ$ , the hysteresis shape resembles that observed in S2 (Fig. 2a). The anomalous Hall resistivity ( $\rho_{zx}^A$ ) has been calculated (Supplementary Fig. 6b), with its contour plot as a function of angle shown in Fig. 2e. This plot reveals two distinct boundaries corresponding to the metamagnetic transitions observed in Figs. 2a and 2c. Within the intermediate phase, the prominent  $\rho_{zx}^A$  suggests the angle evolution of the skyrmion-like phase. At  $45^\circ$ , the magnitude of  $\rho_{zx}^A$  is  $1.3 \mu\Omega \text{ cm}$ . Additionally, the AHC and AHA for  $45^\circ$  and  $90^\circ$  have been calculated (Supplementary Figs. 6c and 6d). The AHC reaches maximum values of  $4.3 \times 10^5 \Omega^{-1} \text{ cm}^{-1}$  and  $6.2 \times 10^5 \Omega^{-1} \text{ cm}^{-1}$ , with AHA values of 79% and 59% for  $45^\circ$  and  $90^\circ$ , respectively. These results, summarized in Fig. 2f, further place TbTi<sub>3</sub>Bi<sub>4</sub> among the highest recorded.

### Electronic band structure and the quasi-1D band folding in TbTi<sub>3</sub>Bi<sub>4</sub>

To understand the ultrahigh AHE and the unique transport behavior across the magnetic phase transition, we carried out systematic investigation on the electronic structure of TbTi<sub>3</sub>Bi<sub>4</sub> and its evolution across the magnetic phase transition using ARPES. Figure 3 shows the overall electronic structure measured at in the first AFM phase ( $T_{N2} < T = 6.3 \text{ K} < T_{N1}$ ). From the Fermi surface (FS) mapping [Fig. 3b, with the definition of the Brillouin zone (BZ) and projected BZ are shown in Fig. 3a], three types of FSs can be resolved. The triangular FSs near zone corners ( $\bar{K}$ ,  $\bar{K}'$ ) originate from the Ti  $3d$  orbitals. The quasi-1D FS, which shows minimal dispersion along the  $k_x$  direction, comes from the Tb  $5d$  orbitals, as Tb forms a quasi-1D chain. The inner ellipse comes from the Bi  $6p$  orbitals. These observations are consistent with previous measurements of other  $Ln\text{Ti}_3\text{Bi}_4$  systems [18–21]. The analysis of the band dispersions along the high symmetry directions further details these orbitals (Fig.

3e). The bands originating from Ti 3*d* are characteristic of the kagome lattice formed by Ti atoms, including the Dirac electrons at  $\bar{K}$  and  $\bar{K}'$  points (labelled in Figs. 3c and 3f), van Hove singularities at  $\bar{M}$  and  $\bar{M}'$  points (saddle points labelled as in Figs. 3f and 3g), and flat bands located below the Fermi level (see Supplementary Note 7). The bands originating from the Bi 6*p* orbitals show two branches (Figs. 3b, 3c, 3f and 3g), indicating the effect of strong spin-orbit coupling. The stacked plot of constant energies further indicates the 3D electronic structure of these bands, especially the full dispersion of Dirac bands at  $\bar{K}$  and  $\bar{K}'$  points (Fig. 3d). The measured band structure shows overall agreement with DFT calculation results (Fig. 3e), confirming the orbital characters of the observed bands. Our ARPES experiments demonstrate that the Dirac points, located at approximately 0.05 eV, are very close to the  $E_F$  (Figs. 3c and 3f). Consequently, Dirac fermions significantly contribute to the transport properties of TbTi<sub>3</sub>Bi<sub>4</sub>, as evidenced by our transport experiments (Fig. 1i and Supplementary Fig. 2). These results indicate that the electronic bands derived from 2D kagome bilayers play a crucial role in transport, highlighting the 2D characteristics of TbTi<sub>3</sub>Bi<sub>4</sub>.

Upon closely examining the bands originating from the Tb 5*d* orbitals, we observed significant band folding with an in-plane folding vector of  $q = (1/3, 0, 0)$  and the opening of a hybridization gap at  $k_x = \pm 0.185 \text{ \AA}^{-1}$  (Fig. 4). Figure 4b shows a characteristic cut across the two Tb bands at  $k_y = -0.24 \text{ \AA}^{-1}$ . From the dispersion, we see clear evidence of band folding (folding vector labeled in Figs. 4a, 4b) and a band hybridization gap opening at  $k_x = \pm 0.185 \text{ \AA}^{-1}$ . The same dispersion measured at 30 K (above  $T_N$ ) shows the disappearance of the band folding and the hybridization gap (Fig. 4f). Our systematic temperature-dependent measurement of the cut reveals the closing of the hybridization gap across 20 K (Figs. 4i and 4j), suggesting a close relationship between the band folding and the magnetic phase transition. Furthermore, due to the folding of the quasi-1D electronic structure from the Tb 5*d* bands, the folding-induced hybridization band gap is also quasi-1D (see the schematic in Fig. 4l). Figure 4c shows the measured dispersion along  $k_x = 0.185 \text{ \AA}^{-1}$ , capturing the hybridization gap at all  $k_y$  values as the splitting between the two labeled bands. This hybridization gap disappears at 30 K (see Fig. 4g). From the summarized hybridization gap versus the  $k_x$  plot (Fig. 4k), we find the hybridization gap is largest for  $k_y < -0.25 \text{ \AA}^{-1}$  and becomes smaller for  $-0.25 \text{ \AA}^{-1} < k_y < 0$ . The existence of hybridization gap explains the suppression of intensity at  $E_F$  at large  $k_y$  (indicated by the red arrow in Fig. 4a). The variation of the hybridization band gap aligns with the fact that the FS of the Tb bands becomes parallel

with  $|k_y| > 0.25 \text{ \AA}^{-1}$ , creating better nesting conditions. Moreover, at all  $k_z$  values, the folding and the hybridization gap remain similar (see Supplementary Note 8), suggesting a 2D folding vector. Notably, band hybridization occurs not only in the Tb  $5d$  bands but also in the Bi  $6p$  and Ti  $3d$  bands, as indicated by the signature of band folding and hybridization gap at the same  $k_x$  values in the cuts measured using linearly vertical photon polarization (Fig. 4d and comparison high-temperature cut in Fig. 4h).

The origin of the band folding with a certain  $q$  requires further investigation. Given the absence of any charge order signature at 4.2 K and even 0.35 K from the STM topography measurements (Fig. 1g), we can rule out the possibility of band folding due to charge density waves (CDWs). Instead, we propose that the band folding is due to a spin density wave (SDW) that emerges below  $T_N$ . From the folding vector  $q = (1/3, 0, 0)$ , we postulate a SDW with a wavelength of approximately  $3a \approx 17 \text{ \AA}$  along the Tb chain (Fig. 4m). The corresponding folded Brillouin zone (see the red square in Fig. 4a) effectively explains the observed band folding below  $T_N$ . The observation of band folding and the opening of a hybridization gap below  $T_N$  strongly suggests a strong coupling between the magnetic texture and electronic band structure. As shown in transport measurements (Figs. 1i, j and Figs. 2a–e), distinct AHE and anomalies in MR profiles are observed only when the magnetic field is applied along the Tb zigzag chain, signifying the important role of Tb zigzag chains in transport. Our ARPES data unequivocally demonstrates that the quasi-1D magnetic ordering in the AFM state greatly influences the electronic band structure of Tb in  $\text{TbTi}_3\text{Bi}_4$ . Additionally, the bands derived from the quasi-2D Ti kagome lattice are also modulated (Figs. 4d and 4h). The impact of magnetic ordering on the electronic band structure from Kagome lattices in  $\text{TbTi}_3\text{Bi}_4$  is further evidenced by our thermo-transport experiments (Supplementary Fig. 2). Therefore, our transport and ARPES results consistently show that quasi-1D magnetic ordering can significantly regulate the electronic band structure of  $\text{TbTi}_3\text{Bi}_4$ . This coupling is further enhanced in the presence of magnetic fields, leading to complex anomalous transport with an ultrahigh AHC.

## Discussion

In  $Ln\text{Ti}_3\text{Bi}_4$  compounds, rare-earth engineering can tune the magnetic properties and electronic correlations [16,17]. To date, only a few cases have reported the influence of magnetism on the evolution of the electronic band structure. For example, magnetism-induced band splitting has been



observed in  $\text{SmTi}_3\text{Bi}_4$  [18] and  $\text{NdTi}_3\text{Bi}_4$  [21], while other related compounds show negligible magnetic effects on the electronic band structure [20]. The observations in this work strongly contrast with previous reports, positioning  $\text{TbTi}_3\text{Bi}_4$  as a unique case within the  $\text{LnTi}_3\text{Bi}_4$  family. The difference between  $\text{TbTi}_3\text{Bi}_4$  and its counterparts may be attributed to the much stronger crystalline-electric-field (CEF) effect of  $\text{Tb}^{3+}$ , as evidenced in the magnetization profiles [Fig. 1d and Supplementary 1b]. In other magnetic siblings in the  $\text{LnTi}_3\text{Bi}_4$  family, the magnetic ordering exhibits more than quasi-1D behavior. However, in  $\text{TbTi}_3\text{Bi}_4$ , the strong CEF and single-ion anisotropy confine the magnetic moments of Tb ions along the zigzag chains, making  $\text{TbTi}_3\text{Bi}_4$  behave as a quasi-1D Ising magnet with strong quantum fluctuations [14,15]. As demonstrated in this work, the quasi-1D magnetic ordering plays a crucial role in  $\text{TbTi}_3\text{Bi}_4$ , significantly regulating its electronic band structure. From a band structure perspective, both the quasi-2D band structure derived from kagome bilayers, as observed in other  $\text{LnTi}_3\text{Bi}_4$  compounds [18–21], and the quasi-1D band structure stemming from Tb zigzag chains significantly contribute to the physical properties of  $\text{TbTi}_3\text{Bi}_4$ , highlighting the importance of the mixed dimensionality in its electronic band structure. From a magnetism perspective, the spins of Tb along the zigzag chains are highly dynamic, with quantum fluctuations and frustration under applied magnetic fields potentially leading to a chiral magnetic texture characteristic of a topological-Hall-like effect. This implies the coexistence of quasi-1D and more than 1D magnetic textures under finite magnetic fields, further emphasizing the significance of the mixed dimensionality in the magnetism in  $\text{TbTi}_3\text{Bi}_4$ .

## Conclusions

In this work, by employing thermodynamic, electrical and thermoelectrical transport and ARPES measurements together with DFT calculations, we systematically investigate the magnetic properties, transport properties, and electronic band structure of the newly synthesized titanium-based bilayer kagome metal  $\text{TbTi}_3\text{Bi}_4$ . We identified the mixed dimensionality in both electronic band structure and magnetism play crucial role in regulating the physical properties of  $\text{TbTi}_3\text{Bi}_4$ . In sharp contrast with other  $\text{LnTi}_3\text{Bi}_4$  siblings, our ARPES experiments unequivocally demonstrate the quasi-1D magnetism is strongly coupled with electronic band structure, and the presence of a quasi-1D hybridization gap in the magnetic state due to band folding possibly from an SDW along the Tb chain. More astonishingly,

the strong coupling between them results in a record-high anomalous Hall conductivity of  $6.2 \times 10^5 \Omega^{-1} \text{ cm}^{-1}$ . These findings emphasize the crucial role of mixed dimensionality and the strong coupling between magnetic texture and electronic structure in regulating physical properties of materials, offering new strategies for designing materials for future spintronics applications.

## Methods

### Sample preparation

TbTi<sub>3</sub>Bi<sub>4</sub> single crystals were grown using a self-flux method with an elemental ratio of Tb:Ti:Bi of 1.2:3:20. Tb (99.95%), Ti (99.99%), and Bi (99.999%) were cut into small pieces, mixed, and placed in an alumina crucible. The crucible was then sealed in a quartz tube under partial argon pressure. The sealed tube was heated to 1,050 °C over 12 hours and maintained at that temperature for 24 hours. It was then slowly cooled to 400 °C at a rate of 2 °C per hour. Single crystals were obtained by removing the flux through centrifugation.

### ARPES measurements

High-resolution ARPES measurements were performed at beamlines BL5-2 of the Stanford Synchrotron Radiation Light Source (SSRL) and beamline BL03U of Shanghai Synchrotron Radiation Facility (SSRF) with Scienta DA30 analyzer. The photon-energy ranges of data acquisition are 40–80 eV. The samples were cleaved *in situ* at  $\sim 7$  K and measured in ultrahigh vacuum with a base pressure of better than  $5 \times 10^{-11}$  Torr. The energy and momentum resolution were 10 meV and  $0.1^\circ$ , respectively.

### STM measurements

The scanning tunneling microscopy (STM) measurements have been performed using a Unisoku USM-1300 system, with a base pressure of  $1.0 \times 10^{-10}$  Torr. The samples were cleaved mechanically *in situ*, and then immediately inserted into the STM head. Topographic images were obtained with Pt/Ir tips with  $V = 1$  V,  $I = 200$  pA.  $dI/dV$  spectra were collected using a standard lock-in technique at a frequency of 973.137 Hz.

### DFT calculation

Our calculations are performed using the projector augmented wave method [34,35] as implemented in the Vienna *ab initio* Simulation package [36,37]. Experimental lattice structure is adopted in our calculations. The exchange-correlation functional is treated within a generalized gradient approximation parametrized by Perdew, Burke, and Ernzerhof [38]. In the self-consistent calculations, the cutoff energy for the plane-wave expansion is 500 eV, and the  $k$ -point sampling grid of the Brillouin zone is  $5 \times 6 \times 7$ . To simulate the paramagnetic state, the  $4f$  electrons of Tb are treated used as core electrons.

### **Electrical, thermoelectrical transport, and thermodynamic measurements**

For transport measurements, a single crystal was cut into a bar shape. A standard six-probe method was used for the longitudinal resistivity and transverse Hall measurements. For thermoelectrical transport measurements, the Seebeck and Nernst signals were measured simultaneously, and the temperature gradient ( $\Delta T$ ) was determined by a type-E thermocouple. Electrical and thermoelectrical transport data were collected in a physical property measurement system (PPMS, Quantum Design). Magnetic susceptibility and specific heat measurements were performed in a magnetic property measurement system (MPMS, Quantum Design) and a PPMS, respectively.

### **Data availability**

The data that support the findings of this study are available from the corresponding authors upon request.

### **References**

- [1] Balents, L. *et al.* Spin liquids in frustrated magnets. *Nature* **464**, 199–208 (2010).
- [2] Inosov, D. S. Quantum magnetism in minerals. *Adv. Phys.* **67**, 149-252 (2018).
- [3] Balents, L. & Savary, L. Quantum spin liquids: a review. *Rep. Prog. Phys.* **80**, 016502 (2017).
- [4] Chamorro, J. R., McQueen, T. M. & Tran, T. T. Chemistry of quantum spin liquids. *Chem. Rev.* **121**, 2898–2934 (2021).
- [5] Nagaosa, N., Sinova, J., Onoda, S., MacDonald, A. H. & Ong, N. P. Anomalous Hall effect. *Rev. Mod. Phys.* **82**, 1539–1592 (2010).

- [6] Liu, E. K. *et al.* Giant anomalous Hall effect in a ferromagnetic kagome-lattice semimetal. *Nat. Phys.* **14**, 1125–1131 (2018).
- [7] Zhao, K., Tokiwa, Y., Chen, H. & Gegenwart, P. Discrete degeneracies distinguished by the anomalous Hall effect in a metallic kagome ice compound. *Nat. Phys.* **20**, 442–449 (2024).
- [8] Yin, J.-X. *et al.* Quantum-limit Chern topological magnetism in  $\text{TbMn}_6\text{Sn}_6$ . *Nature* **583**, 533–536 (2020).
- [9] Yin, J.-X., Lian, B. & Hasan, M. Z. Topological kagome magnets and superconductors. *Nature* **612**, 647–657 (2022).
- [10] Wang, Y. J., Wu, H., Mccandless, G. T., Chan, J. Y. & Ali, M. N. Quantum states and intertwining phases in kagome materials. *Nat. Rev. Phys.* **5**, 635–658 (2023).
- [11] Cheng, E. J. *et al.* Tunable positions of Weyl nodes via magnetism and pressure in the ferromagnetic Weyl semimetal  $\text{CeAlSi}$ . *Nat. Commun.* **15**, 1467 (2024).
- [12] Yuan, J. *et al.* Magnetization tunable Weyl states in  $\text{EuB}_6$ . *Phys. Rev. B* **106**, 054411 (2022).
- [13] Liu, W. L. *et al.* Spontaneous ferromagnetism induced topological transition in  $\text{EuB}_6$ . *Phys. Rev. X* **129**, 166402 (2022).
- [14] Steiner, J. V. M. & Windsor, C. Theoretical and experimental studies on one-dimensional magnetic systems. *Adv. Phys.* **25**, 87 (1976).
- [15] Bertini, B. *et al.* Finite-temperature transport in one-dimensional quantum lattice models. *Rev. Mod. Phys.* **93**, 025003 (2021).
- [16] Ortiz, B. R. *et al.* Evolution of highly anisotropic magnetism in the titanium-based kagome metals  $\text{LnTi}_3\text{Bi}_4$  (Ln:  $\text{La} \cdots \text{Gd}^{3+}$ ,  $\text{Eu}^{2+}$ ,  $\text{Yb}^{2+}$ ). *Chem. Mater.* **35**, 9756–9773 (2023).
- [17] Chen, L. *et al.* Tunable magnetism in titanium-based kagome metals by rare-earth engineering and high pressure. *Commun. Mater.* **5**, 73 (2024).
- [18] Zheng, Z. *et al.* Anisotropic magnetism and band evolution induced by ferromagnetic phase transition in titanium-based kagome ferromagnet  $\text{SmTi}_3\text{Bi}_4$ . Preprint at <https://arxiv.org/abs/2308.14349> (2023).
- [19] Sakhya, A. P. *et al.* Observation of multiple flat bands and topological Dirac states in a new

titanium based slightly distorted kagome metal  $\text{YbTi}_3\text{Bi}_4$ . Preprint at <https://arxiv.org/abs/2309.01176> (2023).

- [20] Jiang, Z. *et al.* Direct observation of topological surface states in the layered kagome lattice with broken time-reversal symmetry. Preprint at <https://arxiv.org/abs/2309.01579> (2023).
- [21] Hu, Y. *et al.* Magnetic-coupled electronic landscape in bilayer-distorted titanium-based kagome metals. Preprint at <https://arxiv.org/abs/2311.07747> (2023).
- [22] Ortiz, B. R. *et al.* New kagome prototype materials: discovery of  $\text{KV}_3\text{Sb}_5$ ,  $\text{RbV}_3\text{Sb}_5$ , and  $\text{CsV}_3\text{Sb}_5$ . *Phys. Rev. Mater.* **3**, 094407 (2019).
- [23] Yang, H. *et al.* Titanium-based kagome superconductor  $\text{CsTi}_3\text{Bi}_5$  and topological states. Preprint at <https://arxiv.org/abs/2209.03840> (2022).
- [24] Werhahn, D. *et al.* The kagomé metals  $\text{RbTi}_3\text{Bi}_5$  and  $\text{CsTi}_3\text{Bi}_5$ . *Z. Naturforsch. B* **77**, 757–764 (2022).
- [25] Phillips, P. W., Hussey, N. E. & Abbamonte, P. Stranger than metals. *Science* **377**, eabh4273 (2022).
- [26] Kuroda, K. *et al.* Evidence for magnetic Weyl fermions in a correlated metal. *Nat. Mater.* **16**, 1090–1095 (2017).
- [27] Hu, J., Rosenbaum, T. F. & Betts, J. B. Current jets, disorder, and linear magnetoresistance in the silver chalcogenides. *Phys. Rev. Lett.* **95**, 186603 (2005).
- [28] Coleman, R. V. & Isin, A. Magnetoresistance in iron single crystals. *J. Appl. Phys.* **37**, 1028 (1966).
- [29] Tokura, Y., and Kanazawa, N., Magnetic skyrmion materials. *Chem. Rev.* **121**, 2857–2897 (2021).
- [30] Neubauer, A. *et al.* Topological Hall effect in the A phase of  $\text{MnSi}$ . *Phys. Rev. Lett.* **102**, 186602 (2009).
- [31] Kurumaji, T. *et al.* Skyrmion lattice with a giant topological Hall effect in a frustrated triangular-lattice magnet. *Science* **365**, 914–918 (2019).
- [32] Wei, W.-S., He, Z.-D., Qu, Z. & Du, H.-F. Dzyaloshinsky–Moriya interaction (DMI)-induced magnetic skyrmion materials. *Rare Met.* **40**, 3076–3090 (2021).
- [33] Yao, X. H. *et al.* Large topological Hall effect and spiral magnetic order in the Weyl semimetal  $\text{SmAlSi}$ . *Phys. Rev. X* **13**, 011035 (2023).

- [34] Blöchl, P. E. Projector augmented-wave method. *Phys. Rev. B* **50**, 17953 (1994).
- [35] G. Kresse and D. Joubert, From ultrasoft pseudopotentials to the projector augmented-wave method. *Phys. Rev. B* **59**, 1758 (1999).
- [36] Kresse, G. & Furthmüller, J. Efficiency of *ab-initio* total energy calculations for metals and semiconductors using a plane-wave basis set. *Comput. Mater. Sci.* **6**, 15–50 (1996).
- [37] Kresse, G. & Furthmüller, J. Efficient iterative schemes for *ab initio* total-energy calculations using a plane-wave basis set. *Phys. Rev. B* **54**, 11169–11186 (1996).
- [38] Perdew, J. P., Burke, K. & Ernzerhof, M. Generalized gradient approximation made simple. *Phys. Rev. Lett.* **77**, 3865–3868 (1996).

## Acknowledgments

This work is supported by the DFG-Projektnummer (No. 392228380) and ERC Advanced Grant No. (742068) “TOP-MAT” for funding. E.J.C. acknowledges the financial support from the Alexander von Humboldt Foundation. Z. K. Liu acknowledges the support from the National Natural Science Foundation of China (92365204, 12274298) and the National Key R&D program of China (Grant No. 2022YFA1604400/03).

## Author Contributions

E.J.C. grew the single crystal, and conducted magnetization, electrical and thermoelectric measurements. K.P.W., Z.K. L., H.K.C., Y.W.L., M.X.W., Y.L.C. and Z.K.L. conducted ARPES and STM experiments and analysis. S.M.N. performed the DFT calculations. T.P.Y., H.B. and V.H. helped to resolve the crystal structure. R.K. and W.S. helped to measure heat capacity. E.J.C. analyzed the transport data with the discussion of Y.X. E.J.C., Z.K.L., and C.F. supervised the project. E.J.C. and K.P.W. contributed equally to this work. E.J.C. wrote the paper with input from all coauthors.

## Competing interests

The authors declare no competing interests.

## Additional Information

**Supplementary information** is available for this paper at the URL inserted when published.

**Correspondence** and requests for materials should be addressed to E.J.C.

(Erjian.Cheng@cpfs.mpg.de), Z.K.L. (liuzhk@shanghaitech.edu.cn), or C.F.  
(Claudia.Felser@cpfs.mpg.de).

**Figure 1**

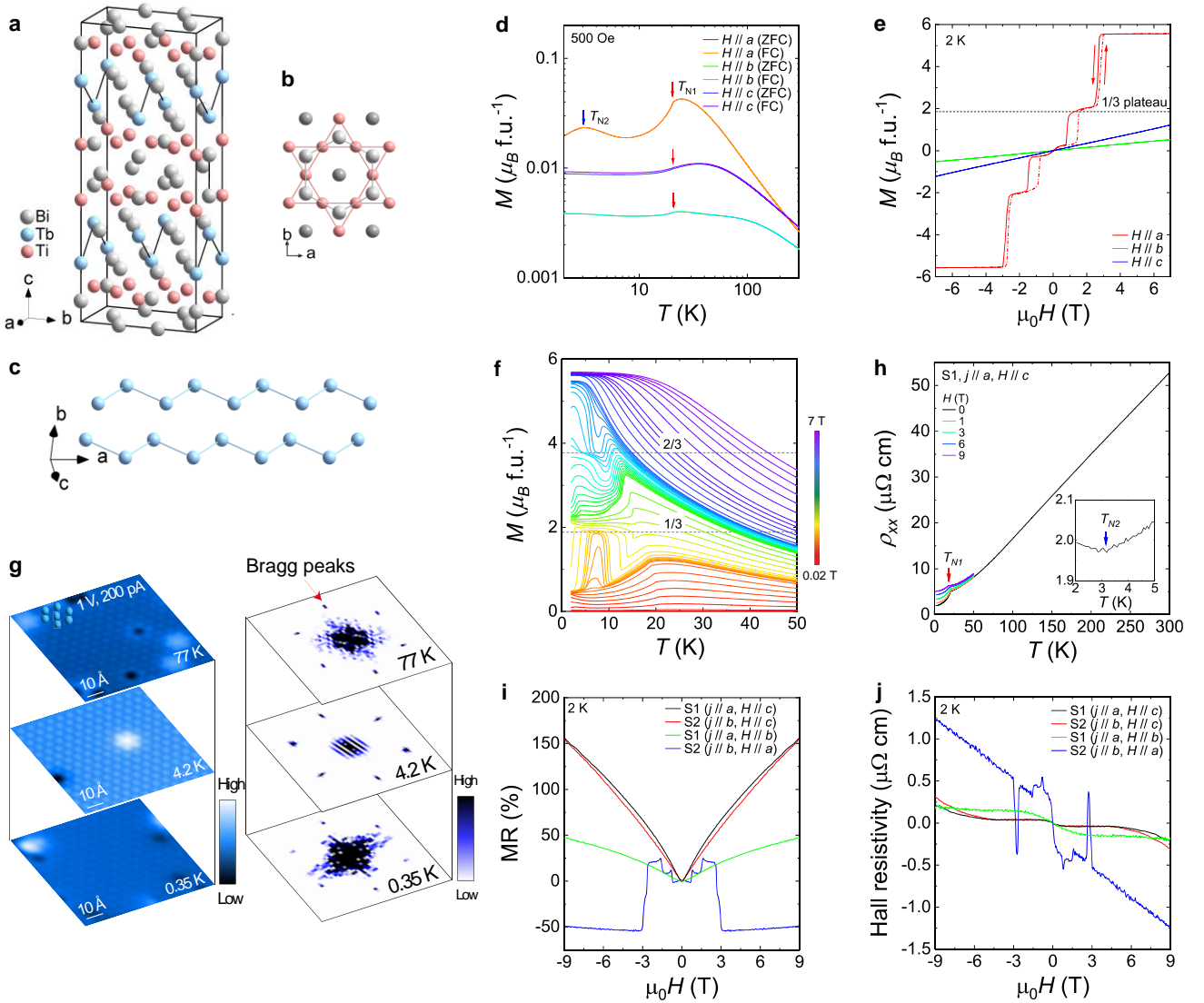


**Figure 1 | Crystal structure and basic properties of  $\text{TbTi}_3\text{Bi}_4$ .** Side view (a), bottom view (b), and (c) the Tb zigzag chain of the  $\text{TbTi}_3\text{Bi}_4$  crystal structure, respectively. (d) Magnetization with magnetic field applied in different orientations during both zero-field cooling and field cooling processes. There are two magnetic transitions located at 20.4 K ( $T_{N1}$ ) and 3 K ( $T_{N2}$ ), respectively. (e) Field-dependent magnetization (MH) at 2 K for magnetic field applied in different orientations. For the  $a$  axis, magnetization exhibits pronounced hysteresis behavior, with a plateau at approximately 1/3 of the saturated magnetization. (f) Temperature-dependent magnetization with zero-field-cooling process in various magnetic fields. The 1/3 magnetization plateau has been marked. Besides, there is another plateau located at 2/3 magnetization, but not very distinguishable in the MH curve in (e). (g) Scanning



tunneling microscope (STM) topograph of Tb termination measured at 77 K, 4.2 K and 0.35 K, and corresponding Fourier transforms. In both paramagnetic and magnetic states, no distinct charge modulations coming from structural instabilities can be distinguished. The STM topograph is measured with bias voltage of 1 V and tunneling current 200 pA. **(h)** Longitudinal resistivity ( $\rho_{xx}$ ) with current  $j$  and magnetic field applied in the  $a$  and  $c$  axis [Sample 1 (S1)], respectively. The residual resistivity ratio (RRR) is 27, defined as  $\rho_{xx}/\rho_{xx}(3\text{ K})$ . Inset shows the low-temperature data in zero field, which displays a minimum value at  $T_{N2}$ . Magnetoresistance (MR) **(i)** and Hall resistivity **(j)** at 2 K for two samples with different measurement configurations. When magnetic field is applied parallel to the  $a$  axis, MR shows negative values with multiple prominent anomalies. For Hall resistivity with field along the  $a$  axis, multiple peaks emerge, showing the anomalous Hall feature.

**Figure 2**

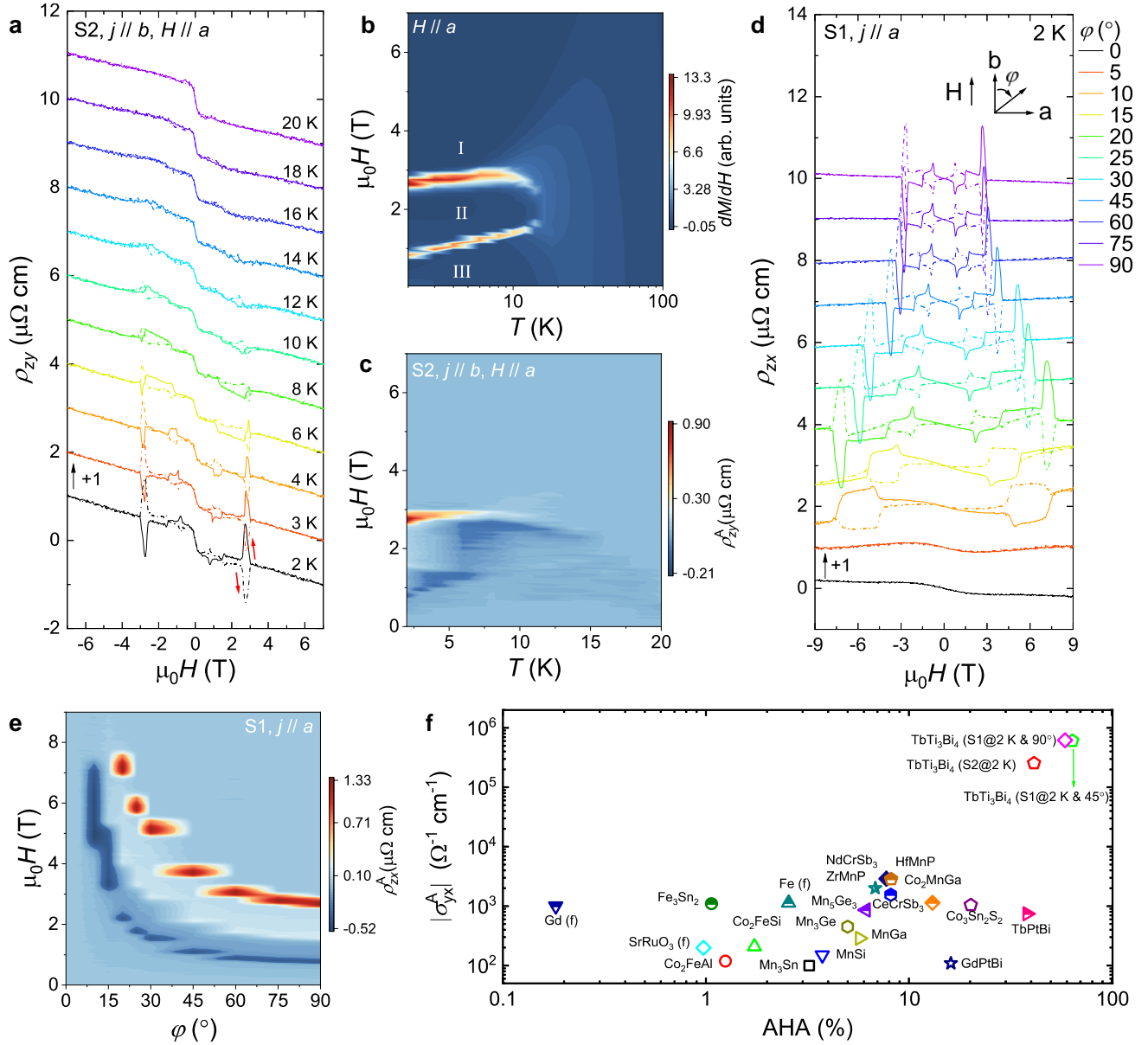


**Figure 2 | Giant anomalous Hall effect in  $\text{TbTi}_3\text{Bi}_4$ .** (a) Transverse Hall resistivity (Sample 2, S2) with current  $j$  and magnetic field applied along the  $b$  and  $a$  axis ( $\rho_{zy}$ ), respectively. The solid and dashed lines represent the field-sweeping process from 9 T to -9 T and -9 T to 9 T, respectively, as indicated by the red arrows. The data has been gradually shifted by  $1 \mu\Omega \text{ cm}$  with increasing temperature for better comparison. (b) Contour plot of field-dependent magnetization. The background color represents the values of the differential of magnetization with respect to magnetic field. (c) Contour plot of the anomalous Hall resistivity ( $\rho_{zy}^A$ ) for S2. The background color represents the values of  $\rho_{zy}^A$ . (d) The anomalous Hall resistivity for S1 with current applied along the  $a$  axis, and magnetic field is

applied in plane.  $\varphi$  represents the angle between the direction of magnetic field and the  $a$  axis. When  $\varphi = 0^\circ$ , magnetic field is parallel to the  $b$  axis. (e) Contour plot of the anomalous Hall resistivity ( $\rho_{zx}^A$ ) for S1. The background color represents the values of  $\rho_{zx}^A$ . (f) Comparison of the magnitude of anomalous Hall conductivity (AHC) versus corresponding anomalous Hall angle (AHA) of TbTi<sub>3</sub>Bi<sub>4</sub> with other reported magnets. For TbTi<sub>3</sub>Bi<sub>4</sub>, the values of AHC are  $2.5 \times 10^5$ ,  $4.3 \times 10^5$  and  $6.2 \times 10^5$   $\Omega^{-1} \text{ cm}^{-1}$  with AHA of 42%, 79%, 59% for S2 at 2 K with  $j // b$  and  $H // a$ , S1 at 2 K with  $j // a$  and  $\varphi = 45^\circ$ , and S1 at 2 K with  $j // a$  and  $\varphi = 90^\circ$ , respectively. The maximum of AHC of TbTi<sub>3</sub>Bi<sub>4</sub> is two orders of magnitude larger than other reported materials.

**Figure 3**

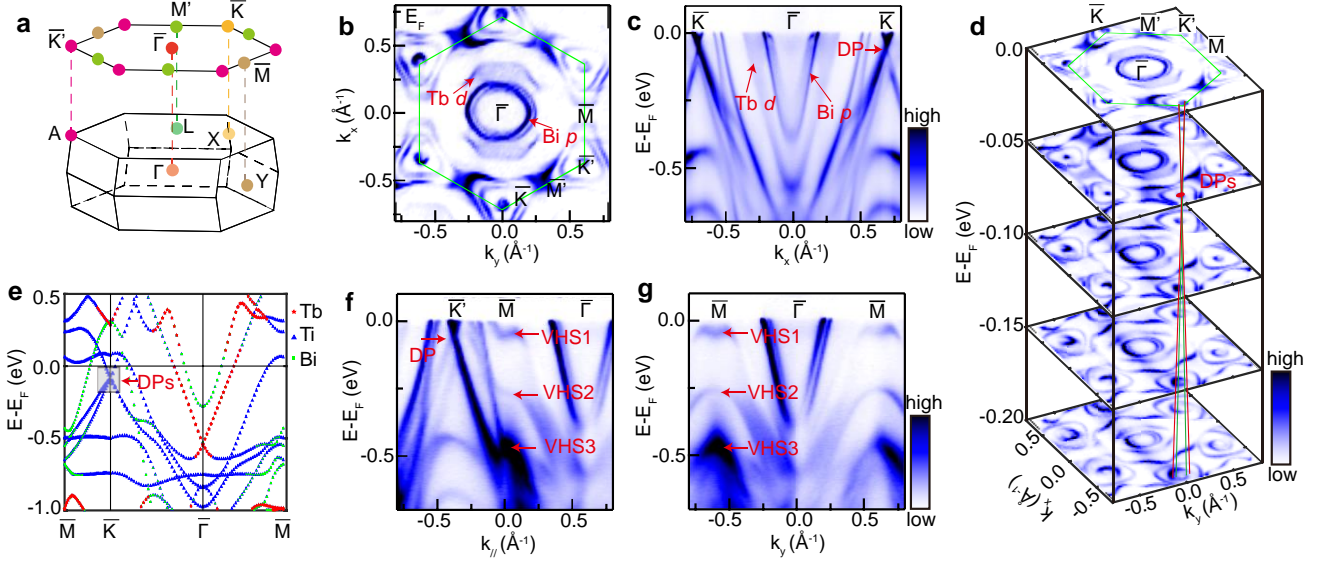


**Figure 3 | Electronic structure of TbTi<sub>3</sub>Bi<sub>4</sub> in AFM state, (a)** Illustration of the 3D Brillouin zone (BZ) of TbTi<sub>3</sub>Bi<sub>4</sub>, and the corresponding (001) surface BZ with the high symmetry points marked. **(b)** Constant energy contour at the Fermi energy of TbTi<sub>3</sub>Bi<sub>4</sub>. The band structure is measured with 46 eV photons with LH polarization, at  $T \sim 6.3$  K. **(c)** Intensity plots of the band dispersion along the  $\bar{K} - \bar{\Gamma} - \bar{K}$  direction. The orbital origin of each band is labelled. The Dirac points (DPs) are marked by red arrows. **(d)** Stacked plot of the constant energy contours of TbTi<sub>3</sub>Bi<sub>4</sub>. The Dirac cone and Dirac point are labelled. **(e)** The calculated energy bands along the high symmetry paths in the  $k_z = \pi$  plane with the orbital component labelled. **(f, g)** Intensity plots of the band dispersion along the  $\bar{K}' - \bar{M} - \bar{\Gamma}$ ,  $\bar{M} - \bar{\Gamma} - \bar{M}$  directions. The Dirac points (DPs) and van Hove singularities (vHSs) are marked by red arrows.

**Figure 4**

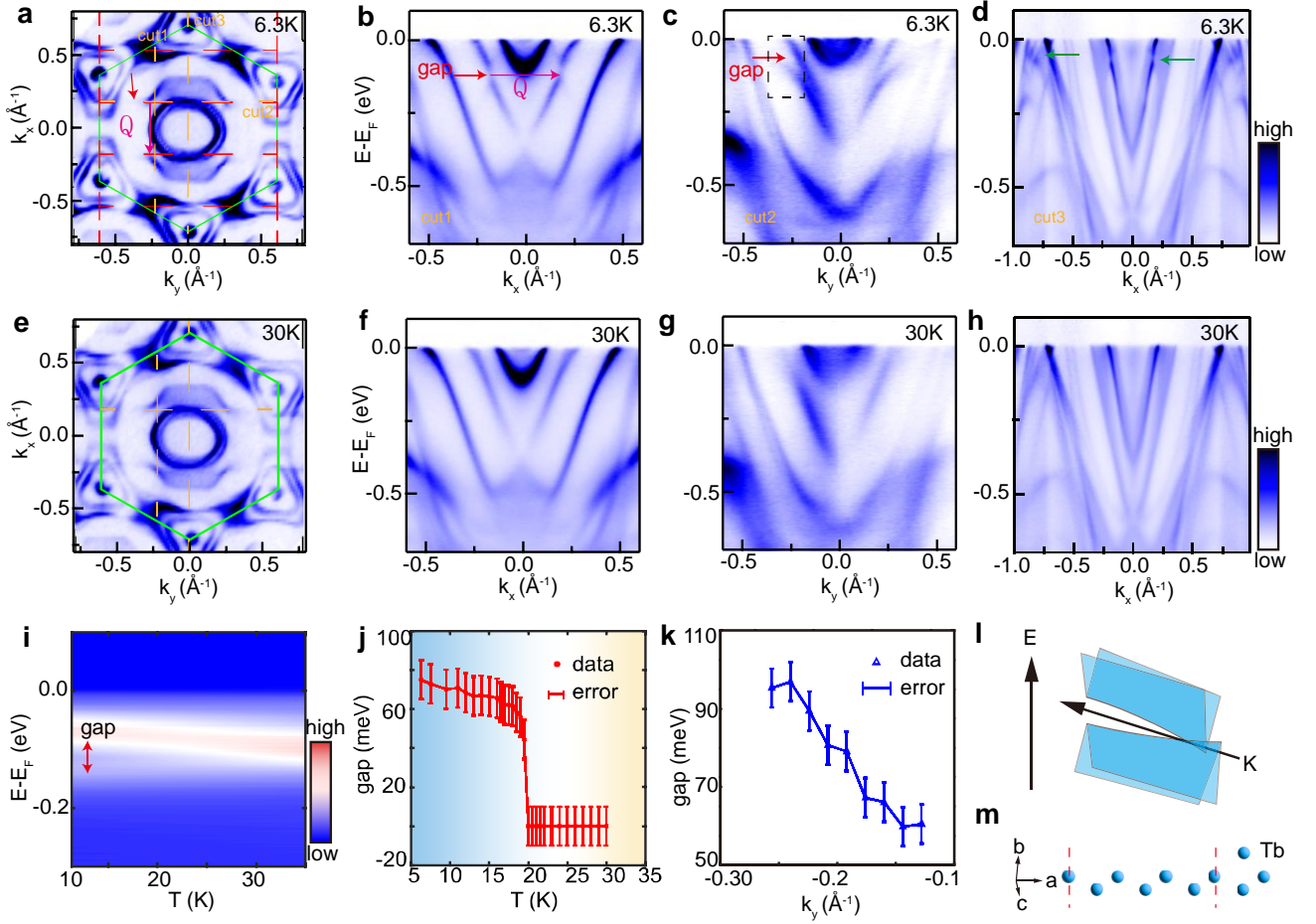


**Figure 4 | Band folding and quasi-1D hybridization gap of  $\text{TbTi}_3\text{Bi}_4$  in the antiferromagnetic (AFM) state.** (a) Constant energy contour at the Fermi level measured with 46 eV, LH polarized photon at 6.3 K. The green and red dashed lines represent the (001) surface Brillouin zone (BZ) and the proposed folded BZ due to spin-wave-density (SDW) order from the Tb chains. The red arrow indicates the suppressed intensity on the Fermi surface in the AFM state due to the hybridization gap near  $E_F$ . Magenta arrow indicates the SDW wave vector. (b-d) The intensity plots of energy bands dispersion along the orange dashed lines in (a). The measured polarization is LH for (b, c) and LV for (d). Red arrow indicates the hybridization gap in the Tb 5d bands, green arrow indicates the band folding/hybridization gap in the Ti 3d and Bi 6p bands. (e) Constant energy contour at the Fermi level measured with 46 eV, LH polarized photon at 30 K. The green dashed lines represent the (001) surface Brillouin zone (BZ). (f-h) are the same as (b-d) but measured at temperature 30 K. (i) Intensity plot of

the energy distribution curve at  $k_x = -0.185 \text{ \AA}^{-1}$  from **(b)** at various temperatures. **(j)** The extracted hybridization gap size versus temperature. **(k)** The evolution of hybridization gap in **(c)** with  $k_y$  momentum. **(l)** The schematic of quasi-1D band folding and the formation of quasi-1D hybridization gap in  $\text{TbTi}_3\text{Bi}_4$ . **(m)** The proposed spin density wave (SDW) along the Tb chain with  $3a$  period.